Opto-Electronic Advances

Supplementary information

July 2023, Vol. 6, No. 7

DOI: 10.29026/oea.2023.220163

Speckle structured illumination endoscopy with enhanced resolution at wide field of view and depth of field

Elizabeth Abraham, Junxiao Zhou and Zhaowei Liu*

Department of Electrical and Computer Engineering, University of California, San Diego, 9500 Gilman Drive, La Jolla, California 92093, United States.

*Correspondence: ZW Liu, E-mail: zhaowei@ucsd.edu

This file includes:

Supplementary information for this paper is available at https://doi.org/10.29026/oea.2023.220163

Section 1: Premise of the two-fiber model

From the above, we see that using single fiber results in an order of reduction in the illumination spatial frequency cutoff compared to the two-fiber case. This will greatly reduce the resolution enhancement possible as given by Eq. 3. The two fibers case will ensure that the complete field of view is maintained much like the standard WLE, but with higher levels of resolution as opposed to single fiber case. The practical estimate results in 75%–80% accuracy between theory and practice for different focal planes.

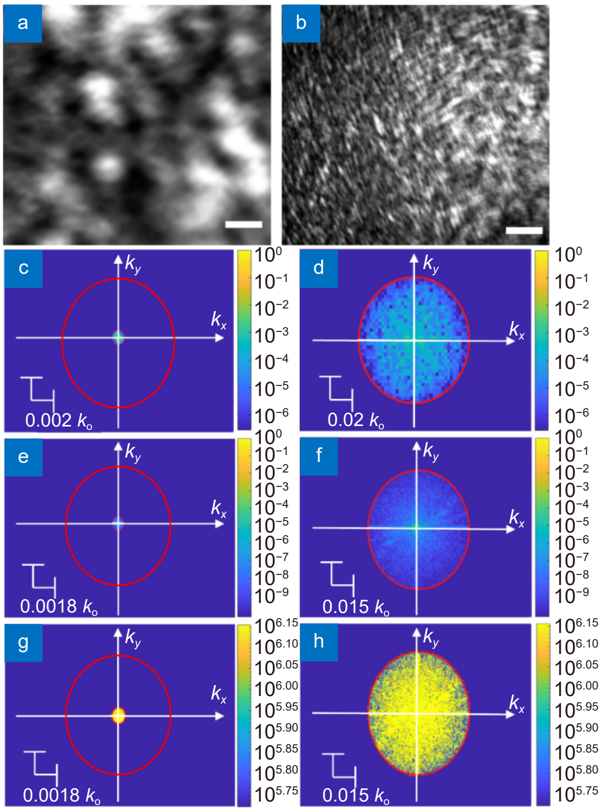

Fig. S1 | Premise of two fiber model. (**a**) Experimental single fiber speckle pattern. (**b**) Experimental two fiber large angle speckle interference pattern. Scale bar (a–b) is 250 μm. (**c**) Theoretical Fourier spectra of single fiber speckle pattern. (d) Theoretical Fourier spectra of two fiber speckle interference pattern. (**e**, **g**) Experimental Fourier spectra of single fiber speckle pattern (a) with different plotting scales between e and g. (**f**, **h**) Experimental Fourier spectra of two fiber speckle interference pattern (b) with different plotting scales between f and h. (a–h) Focal distance: 5.7 cm.

Section 2: Specifications of the SSIE

Unbounded: The SSIE can be sterilized along with that of the WLE. The usage of the SSIE will be unbounded apart from occasional clipping of the fiber tips as and when the fiber tip wears out. However, there would be no need of replacements of the probe itself like in CLE practices.

Any modality: High definition or otherwise.

The illumination NA of the SSIE remains a tunable parameter with respect to the endoscope's working distance. Hence, it would be ideal to place the sample close to the endoscopic image sensor to get the best resolution enhancement as seen under the working principle of the SSIE section. The resolution will be enhanced by the employment of the SSIE compared to the WLE's basic white light equivalent (Table 1).

The specifications of WLE's and CLE's from the table can be found[S1–S3].

Table S1 | Specifications of the SSIE compared with other models of endoscope.

Specifications	WLE (Any modality*)	CLE	SSIE
Field of View	90–170°	240–600 μm	As that of WLE
Resolution	Diffraction limit of the system	Diffraction limit of the system	2–4.5 times the diffraction limit of the system
Depth of Field	~1.5– ~100 mm	40–70 μm	As that of WLE
Maximum Number of Uses	Unbounded	10–20	Unbounded*

Section 3: Schematic of the vibrational motor

The step motor is attached to the fiber via the kink as shown to stretch the fiber spool during image acquisition.

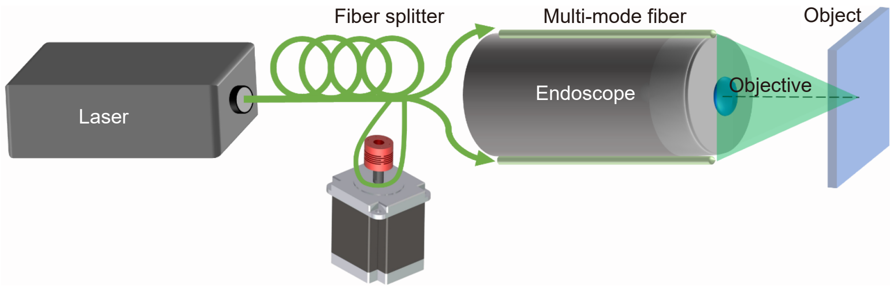

Fig. S2 | Schematic of the step motor.

Section 4: Calibration and characterization

Group 1 and group 2 elements of the USAF target are imaged for distance of 5.7 cm. With the knowledge of the feature size in the USAF target and the distance profile from the cross sectional intensity curve (Fig. S3(c)), the image pixel resolution can be measured[S4,S5].

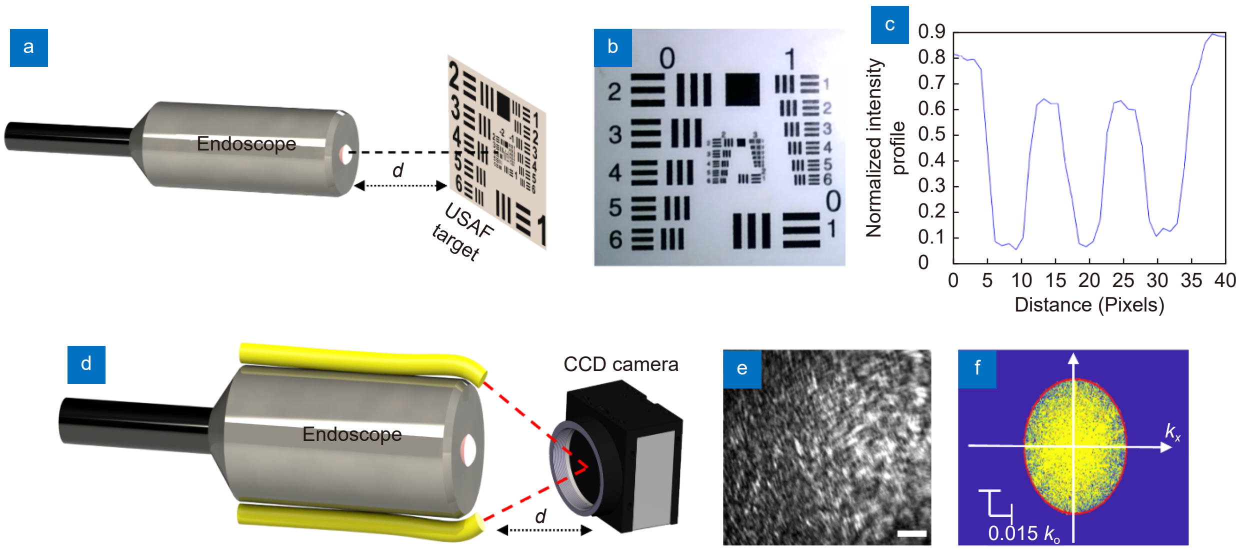

Fig. S3 | (**a**–**c**) Imaging calibration of the USAF. (**a**) Schematic of the USAF acquired by the endoscope. (**b**) USAF image. (**c**) Normalized intensity profile of group 2, element 1 at distance *d*=5.7cm. (**d**–**f**) Schematic of speckle NA estimation. (**d**) Schematic of speckle illumination acquired by the CCD camera. (**e**) Speckle interference pattern at distance *d*=5.7cm. (**f**) Fourier spectra of (e).

With the knowledge of the specifications of the CCD camera, the speckle interference pattern is analyzed in the Fourier domain to estimate the speckle cutoff which gives the speckle NA.

Section 5: Analysis of processing

For a 3D surface, the reconstruction must be done cautiously as the point spread function (PSF) differs across varying planes. Whether it differs significantly or not depends on the depth of examination. Since endoscopes have a large field of view and depth of field, reconstruction with a uniform point spread function will result in errors as illustrated.

The image is segmented into smaller sections as in Fig. S4(h–n), which is then reconstructed using the blind-SIM algorithm. Applying a uniform PSF as in Fig. S4(o–u) to realize the whole 3D image results in errors in the reconstruction as indicated in Fig. S4(a–g). These changes degrade and affect the reconstructed images quality. In our future explorations we would consider approaches for extracting depth information prior with stereoscopic approaches and deep learning approaches, so that the segmentation may be more directed[S6,S7]. With this knowledge, the segmentation and reconstruction may be assisted better.

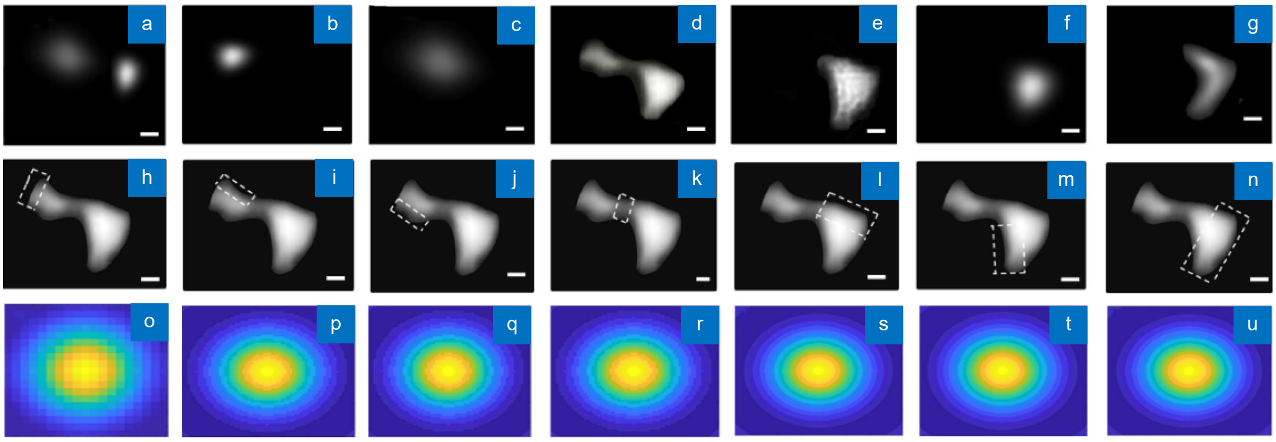

Fig. S4 | Errors in image reconstruction with large depth of field. (**a–g**) Errors in reconstruction due to the application of a uniform point spread function (PSF). (**h–n**) Diffraction limited images with regions of varying PSF's as indicated by dashed boxes. (**o–u**) Representation of varying point spread functions (PSF) for different regions indicated in (h–n). Scale bar is 700 μm.

Section 6: Schematic for high-speed imaging

As for the imaging speed of the SSIE, currently we utilize randomly varying high-resolution speckle illuminations for enhancing image resolution. In our experiments, data was recorded in a series of 120 frames or lower. Frames were acquired at a rate of one frame per second as a few milliseconds within the second timeframe are accounted for the speckle pattern to settle after the multimode fiber has been modulated. The acquisition took about three minutes. In our future studies we will explore employing the spatial light modulator (SLM) to explore the pathway to high-speed imaging. A schematic for which is shown below.

The idea on how to use pre-determined speckle illumination for high-speed imaging has been illustrated in ref.[S8]. In the paper, it is demonstrated that the pre-determined speckles represent much more prior information enabling improved image reconstruction with less measurements via compressive sensing. This will lead to higher imaging speed. In our future efforts, we intend to employ the spatial light modulator (SLM) to generate pre-determined specular patterns for high-speed imaging. By employing the SLM along with a faster GPU (NVIDIA GeForce or the Nvidia Titan V), a complete demonstration of the high-speed super-resolution imaging of the SSIE for clinical practices can be explored. Since the detailed experiment is out of the scope of this current work, this will be undertaken by us in future studies.

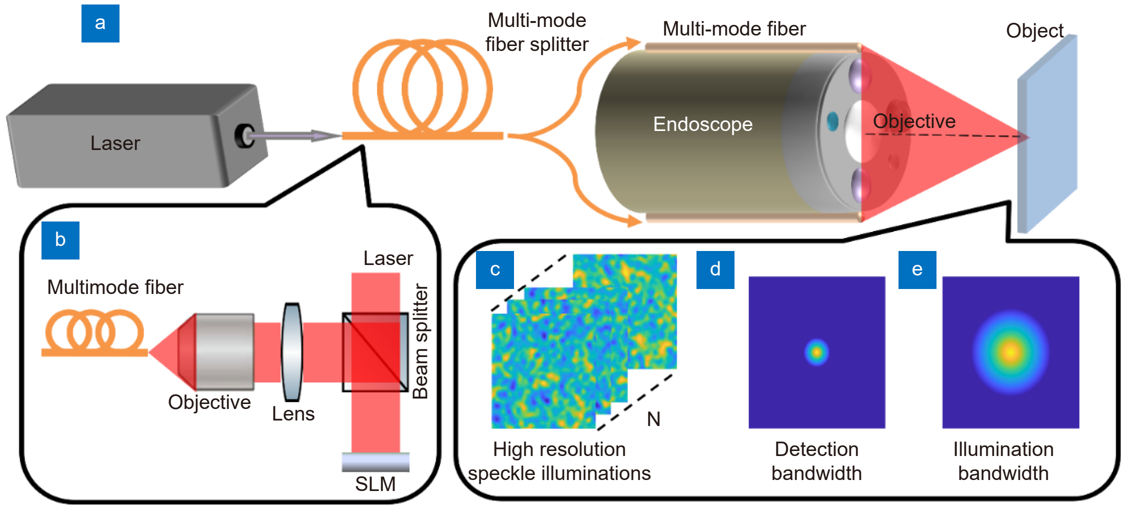

Fig. S5 | Schematic of SLM based illumination patterns for high-speed SSIE imaging. (**a**) Schematic of the setup. (**b**) Speckle generation via a spatial light modulator. (**c**) N frames containing high resolution speckles for reconstruction. (**d**) Schematic of detection bandwidth. (**e**) Schematic of illumination bandwidth.

Section 7: Flowchart of process

A GUI handle for the physician or the user will enable an automated operation of the process of SSIE, for which the flowchart is shown below. The handle will function as a user interface to the clinician to switch between WLE and SSIE modality.

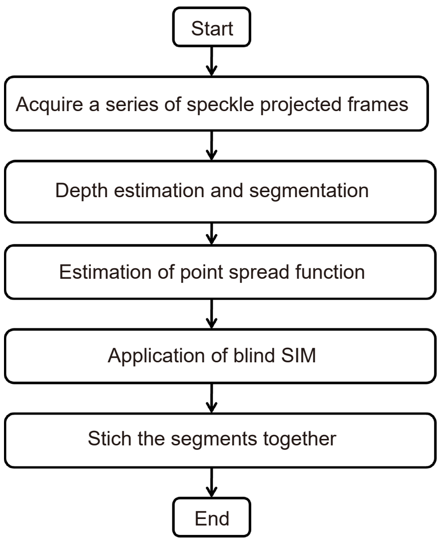

Fig. S6 | Flowchart of the process.

Section 8: Future efforts: Towards a clinical SSIE

The approach in this paper concentrates on implementing the SSIE in a fluorescent specimen. Fluorescent imaging in GI endoscopy is prevalently practiced clinically[S9–S11]. Hence, the SSIE will help strengthen and bolster such practices. The SSIE's performance is independent of the specimen, which includes securing of a particular type, nature, or concentration of specimen. Any fluorescent dye used in GI endoscopy can be employed to visualize the performance of the SSIE. As for dye delivery, the endoscopic probe itself is utilized to deliver the dye to the GI tract. Similarly, spray catheters or water pump systems attached to the colonoscope are also utilized to deliver dyes to the GI tract as is prevalent in chromoendoscopic practices[S12,S13]. As for the SSIE's approach in a coherent setting, we anticipate that the SSIE will produce about 2x resolution enhancement from preliminary results. However, it is something that we would like to explore in our future efforts. This paper deals with the proof of concept of the SSIE in an incoherent setting which has been successfully demonstrated, future efforts will be directed towards exploring the SSIE's performance on clinical specimens and in a clinical setting. During the clinical employment of the SSIE, frames may be affected by motion due internal or external movements. This can be rectified by motion alleviating mechanisms[S14–S18]. In our prior studies of correcting motion in GI images, we observe that the intensity-based image registration works best to correct any potential movements in such scenarios with good accuracy, capable of correcting endoscopic movements (scope movements + body movements) and breathing movements which also appears as a form of displacement. In addition, the intensity-based registration has also been implemented before to rectify motion brought about by human respiration successfully (breathing)[S19–S21]. Before proceeding to the SSIE reconstruction, the acquired images will be subjected to the intensity-based image registration to avoid dynamic artifacts. If needed, additional models of image registration may be explored as part of our future works for a clinical translation of the SSIE. Additionally, in the blind-sim algorithm a secondary alignment using the alignment operation (Table S2) is performed which would ensure that the possibility of such dynamic artifacts to be further capped. Since we would focus on high-speed imaging as part of our future works, the image acquisition will also be speed up relatively faster. Hence the range of such occurrences of drastic motion may be reduced to a much narrower time range. For motion in GI endoscopy, intensity-based image registration approaches would work best as observed from our earlier studies[22]. With high-speed imaging, image acquisition will be speed up considerably, which extensive motion correction may not be necessarily needed. The different frame numbers in Fig. 4 and Fig. 5 are to indicate that the reconstruction remain unaffected with reduced number of frames where the oversampling factor alpha can be reduced to less than 10 while imaging at the same focal plane. The value of the oversampling factor is currently realized by experimental estimation. A more robust realization of the oversampling factor with respect to the number of frames will be explored in our future efforts. In addition, with the high-speed imaging, the oversampling factor would not be a major over bearer to the process itself. From the 3D curved surface demonstrations in this paper, we denote that the SSIE can successfully reconstruct a 3D sample. 3D images are in effect 2D images when acquired by any image sensor, wherein the depth information is encoded into the 2D frame. Knowledge of the depth of the sample as prior information may be further helpful in reconstruction (as seen in Section 5). As such, the blind-SIM approach of the SSIE is robust to the nature, type, shape, or size of the sample or that of the system itself. This gives us a great degree of freedom in its usage and its translation into a clinical setting becomes fairly straightforward.

Section 9: Blind-SIM algorithm process

All supporting equations used for reconstruction in the blind-sim process have been given in the ref.[25] in the main file.

Table S2 | Blind-sim process.

Steps	Breakdown
Mode	Run the algorithm on GPU of device to save on processing time
File path	Specify file path in which the acquired frames reside, by specifying the type of file acquired
Create save location	Specify the folder in which the processed frame and other relevant files will be stored
Read data	Read the acquired frames from the folder in which it is stored at
Specify reconstruction parameters	Parameters Specify number of iterations (60–80 used for this study) Specify step size (step size of ~5 used in this study) Specify interpolation factor and conjugate gradient descent parameters Specify zero padding width (1, used in this study) Specify an option to save processed figures Specify conjugate gradients initial step size (2e-5 used in this study)
Specify experimental parameters	Specify numerical aperture Specify magnification Specify the wavelength used Specify pixel size specifications
Length	Estimate the length of the frames in the folder from which it is read
Align	Align sub frames with circular shift operation
Diffraction limited image	Estimate the mean of the sub frames and save figure in the save location
Crop	Select area to crop to be used for reconstruction by specifying the needed co-ordinates
Mitigate noise	Select area of background noise Apply Weiner filtering to mitigate noise Subtract noise value from the selected region Plot sub frames after noise removal
Boundary effect	Apply Hanning window to avoid boundary effects
Image area	Interpolate image area by bicubic method Correct for interpolation overshoot if present Plot the post interpolated sub frames
Point spread function (PSF)	Define PSF by the standard point spread function formula which includes the numerical aperture, magnification and pixel parameters specified in step 5 Plot the PSF figure
Prepare for reconstruction	Define an initial guess of the average illumination Define an initial guess at the object/sample in accordance with equations in ref.[25]
Iteration parameters	Specify iteration parameters which include the conjugate gradient initial step, gamma, the weights needed in accordance with equations in ref.[25]
Iterative reconstruction	For 1=1: *N* (number of iterations) Begin iterative reconstruction process with the parameters Calculate residual error (Eq. S4 (supplementary file): ref.[25], main file) Perform FFT based 2D convolution as a part of the calculation of the residual error Define cost function (Eq. S12 (supplementary file) : ref.[25], main file) Define gradients (Eq. S14 (supplementary file): ref.[25], main file) Guarantee gradient descent direction Continue the reconstruction process with the gradients defined
Estimate certain parameters	Estimate alpha(ref.[25], main file) Re-calculate the cost function (Eq. S12 (supplementary file): ref.[25], main file)
Update parameters	Update parameters used to calculate the object/sample Update the processed object frame Generate the processed frame
Super resolution frame	Plot the super resolution result Plot the Fourier transform of the reconstruction result and intensity comparison plots
Save figure and plots	Save the reconstruction results in the location given in step 3

Section 10: Reasons to choose the blind-sim process

Table S3 | Differences between traditional and blind sim.

Traditional SIM	Blind-SIM
Enhances image resolution up to 2 times	Enhances image resolution greater than 2 times, as indicated in this study
Can be applied to planar objects	Can be applied to planar and non-planar objects
Illumination will be distorted, blurred and hard to predict when cast onto a non-planar surface	Illumination will not be affected when cast onto a non-planar surface as it follows a random specular nature
Not easily translatable to dynamic systems such as endoscopes where strict control of illumination patterns, focusing optics and calibration protocols are preferred	Easily translatable to dynamic systems as strict control of illumination patterns, focusing optics and calibration protocols are not needed
Limited depth of field	Depth of field is vast as shown in this study and can be extended to as large as WLE may allow
Spatially structured patterns of light are used for illuminating the sample	Random specular illuminations are used for illuminating the sample

Section 11: Preparation of the fluorescent stain samples

The dye used was Rhodamine 6G which was diluted against ethanol at 8 mg/mL concentration. This is drop casted on a glass slide using a pipette. The dye appears moderately pink in color when mixed in with ethanol. When illuminated with a laser source of wavelength of 532 nm's used in this study, the Rhodamine 6G emits fluorescent light around 560 nm. When it is recorded by a colorful camera, the image appears yellow.

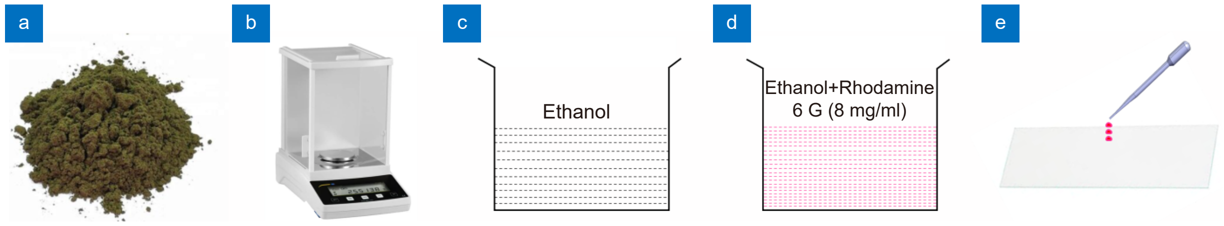

Fig. S7 | Schematic of the preparation of the fluorescent stain samples. (**a**) Powder of Rhodamine 6G dye. (**b**) The Rhodamine 6G dye is weighed on a laboratory high precision scale at 8 mg. (**c**) Schematic of a transparent ethanol solution. (**d**) Schematic of the mixture of the ethanol with rhodamine 6G powder at 8 mg/ml. (**e**) Schematic of the rhodamine dye being drop casted onto transparent glass slide.

Section 12: Quantitative comparisons

The quantitative results are obtained by examining the Fourier transform cutoffs of the diffraction limited and enhanced images pertaining to Figs. 3, 4 and 5.

Table S4 | Quantitative results of image resolution enhancement.

Figures	Expected		Obtained	
	Vertical	Horizontal	Vertical	Horizontal
Figure 3	3.51	3.40	3.50	3.39
Figure 4	2.52	2.40	2.50	2.39
Figure 5	2.52	2.41	2.52	2.20
Accuracy % (average)	99.6 (Vertical)			
	96.8 (Horizontal)			

Smaller the brisque score is, lower is the image distortion and higher is the images perceptual image quality. As seen from Table S5, the original undistorted image (ground truth) and the enhanced images have realatively low brisque scores which reflects on its higher perceptual quality in comparison to its diffraction limited counterpart. The enhanced frames indicates good perceptual image quality individually and on average from its diffraction limited counterpart, as noted in Table S5[S23,S24].

Table S5 | Perceptual quality metric (brisque) score comparison.

Figures	Diffraction limited image	Enhanced image
Figure 3	51.3 (Fig. 3(a))	43.9 (Fig. 3(b))
	43.4 (Fig. 3(e), ground truth)	43.4 (Fig. 3(e), ground truth)
Figure 4	53.1(Fig. 4(a))	51.5 (Fig. 4(b))
Figure 5	45.3 (Fig. 5(c))	44.5 (Fig. 5(d))
	43.4 (Fig. 5(b), ground truth)	43.4 (Fig. 5(b), ground truth)
Average % (reduction)	6.7	

References

S1. The American Society for Gastrointestinal Endoscopy. Confocal laser endomicroscopy. *Gastrointest Endosc* **80**, 928–938 (2014).

S2. The American Society for Gastrointestinal Endoscopy. GI endoscopes. *Gastrointest Endosc* **74**, 1–6 (2011).

S3. Wang QZ, Khanicheh A, Leiner D, Shafer D, Zobel J. Endoscope field of view measurement. *Biomed Opt Express* **8**, 1441–1454 (2017).

S4. Rajan DK, Kreutzer J, Välimäki H, Pekkanen-Mattila M, Ahola A et al. A portable live-cell imaging system with an invert-upright-convertible architecture and a mini-bioreactor for long-term simultaneous cell imaging, chemical sensing, and electrophysiological recording. *IEEE Access* **6**, 11063–11075 (2018).

S5. Wang YM, Raj M, Mcguff HS, Bhave G, Yang B et al. Portable oral cancer detection using a miniature confocal imaging probe with a large field of view. *J Micromech Microeng* **22**, 065001 (2012).

S6. Abdullah HS, Ahmed SS. Proposed depth image extraction approach for 3D stereoscopic image. (2019).

S7. Eigen D, Puhrsch C, Fergus R. Depth map prediction from a single image using a multi-scale deep network. In *Proceedings of the 27th International Conference on Neural Information Processing Systems* 2366–2374 (MIT Press, 2014). https://dl.acm.org/doi/10.5555/2969033.2969091

S8. Ma Q, Hu H, Huang E, Liu ZW. Super-resolution imaging by metamaterial-based compressive spatial-to-spectral transformation. *Nanoscale* **9**, 18268–18274 (2017).

S9. Tajiri H. Autofluorescence endoscopy for the gastrointestinal tract. *Proc Jpn Acad Ser B Phys Biol Sci* **83**, 248–255 (2007).

S10. Mortensen OE, Nerup N, Thorsteinsson M, Svendsen MBS, Shiwaku H et al. Fluorescence guided intraluminal endoscopy in the gastrointestinal tract: A systematic review. *World J Gastrointest Endosc* **12**, 388–400 (2020).

S11. Hoffman A, Atreya R, Rath T, Neurath MF. Use of fluorescent dyes in endoscopy and diagnostic investigation. *Visc Med* **36**, 95–103 (2020).

S12. Antonelli G, Correale L, Spadaccini M, Maselli R, Bhandari P et al. Dye-based chromoendoscopy for the detection of colorectal neoplasia: meta-analysis of randomized controlled trials. *Gastrointest Endosc* **96**, 411–422 (2022).

S13. Buchner AM. The role of chromoendoscopy in evaluating colorectal dysplasia. *Gastroenterol Hepatol* **13**, 336–347 (2017).

S14. Abouei E, Lee AMD, Pahlevaninezhad H, Hohert G, Cua M et al. Correction of motion artifacts in endoscopic optical coherence tomography and autofluorescence images based on azimuthal en face image registration. *J Biomed Opt* **23**, 016004 (2018).

S15. Kang W, Wang H, Wang Z, Jenkins MW, Isenberg GA et al. Motion artifacts associated with in vivo endoscopic OCT images of the esophagus. *Opt Express* **19**, 20722–20735 (2011).

S16. Abouei E, Lee AMD, Pahlevaninezhad H, Hohert G, Cua M et al. Motion artifacts in endoscopic catheter-based images: simulation and motion correction method. *Proc SPIE* **10711**, 107110E (2018).

S17. Camino A, Zhang M, Dongye CL, Pechauer AD, Hwang TS et al. Automated registration and enhanced processing of clinical optical coherence tomography angiography. *Quant Imaging Med Surg* **6**, 391–401 (2016).

S18. Eldib ME, Hegazy MAA, Cho MH, Cho MH, Lee SY. A motion artifact reduction method for dental CT based on subpixel-resolution image registration of projection data. *Comput Biol Med* **103**, 232–243 (2018).

S19. Mustafa A, Abhilash RH, Chauhan S. Organ movement and targeting during non-invasive therapy and surgery. *SM J Biomed Eng* **3**, 1014 (2017).

S20. Ledesma-Carbayo MJ, Kellman P, Arai AE, McVeigh ER. Motion corrected free-breathing delayed-enhancement imaging of myocardial infarction using nonrigid registration. *J Magn Reson Imaging* **26**, 184–190 (2007).

S21. Mori K, Deguchi D, Sugiyama J, Suenaga Y, Toriwaki J et al. Tracking of a bronchoscope using epipolar geometry analysis and intensity-based image registration of real and virtual endoscopic images. *Med Image Anal* **6**, 321–336 (2002).

S22. Abraham E. Weighting and thresholding-based detail preserving image enhancement of gastrointestinal images with noise suppression. Manuscript Submitted for Publication (2022).

S23. Mittal A, Moorthy AK, Bovik AC. No-reference image quality assessment in the spatial domain. *IEEE Trans Image Process* **21**, 4695–4708 (2012).

S24. Mittal, A., A. K. Moorthy, and A. C. Bovik. "Referenceless image spatial quality evaluation engine." 45th Asilomar Conference on Signals, Systems and Computers. Vol. 38. 2011. (https://scholar.google.com/scholar?cluster=15977832740339101980&hl=en&oi=scholarr https://scholar.google.se/citations?user=t9eduncAAAAJ&hl=th)